



Modelling orthogonal cutting of Ti-6Al-4 V titanium alloy using a constitutive model considering the state of stress

Wenyu Cheng¹ · José C. Outeiro¹

Received: 9 July 2021 / Accepted: 24 November 2021 / Published online: 11 January 2022
© The Author(s), under exclusive licence to Springer-Verlag London Ltd., part of Springer Nature 2021

Abstract

The excellent mechanical and physical properties of Ti6Al4V titanium alloy make it a good candidate material for a broad range of applications, with special relevance for the aerospace industry. As a difficult-to-cut alloy, it represents a great challenge to improve its machinability and surface integrity while simultaneously avoiding the high time consuming and cost of the experiments. Modelling and simulation of the machining process offer a cost-effective method to investigate the machining process. In this work, an orthogonal cutting model of Ti-6Al-4 V alloy was developed and used to simulate the major cutting outcomes, including: forces, temperature distribution, chip geometry, chip compression ratio and residual stresses in the machined surface and subsurface. This cutting model includes a constitutive model accounting for the state of stress and the strain-rate effects on the mechanical behaviour (plasticity and damage) of Ti-6Al-4 V alloy in metal cutting. In addition, Zorev contact model is used to simulate the contact stresses at both tool-chip and tool-workpiece interfaces. The proposed cutting model could predict relatively well the major cutting outcomes for seven cutting conditions. The difference between simulated and experimental cutting forces is less than 14%, but the predicted thrust force is underestimated about 53% in maximum. The difference between simulated and measured maximum compressive residual stresses in cutting and transversal directions can reach in average about 17% and 36%, respectively. The maximum difference between predicted and measured thicknesses of the layer affected by residual stresses is less than 19%. This study highlights several critical points affecting the thrust force and the residual stress predictions, which should be considered in future developments of cutting models.

Keywords Metal cutting · Simulation · Ti-6Al-4 V · Constitutive model

1 Introduction

More than 100 titanium alloys are known, although only about 20 to 30 have reached commercial applications [1]. The traditional Ti-6Al-4 V titanium alloy is the most used, covering about 50% of the existing applications [1]. Ti-6Al-4 V titanium alloy is a α - β alloy that contains both α and β stabilisers, and a microstructure combining α (hcp) and β (bcc) phases. This alloy can be heat treated to increase its strength (tensile strength of 1035 MPa after solution treatment and aging), especially for high temperature (between 350 °C and 400 °C) applications [1]. This alloy is used in several applications, including aerospace, due to their

excellent mechanical properties, such as high strength/weight ratio and high creep and corrosion resistances.

The key challenges faced in the aerospace sector were to improve process efficiency and cost without reducing the functional performance and life of workpiece (corrosion resistance, fatigue lifespan, etc.), which is controlled by the surface integrity. Thus, in order to tackle these challenges, the cutting conditions should be optimized, including cutting tool geometry/material, cutting regime parameters, metal working fluid and so on.

Machinability and surface integrity of titanium alloys have been investigated by many researchers using both experimental and modelling methods, and several reviews have been published [2–6]. The high strength (high cutting forces), high chemical reactivity (high adhesion to the cutting tool) and low thermal conductivity (high local temperatures at the tool-chip interface) of these alloys are the main factors responsible for its low machinability [7]. In addition,

✉ José C. Outeiro
jose.outeiro@ensam.eu

¹ Arts Et Metiers Institute of Technology, LaBoMaP, HESAM University, Rue Porte de Paris, 71250 Cluny, France

its low Young modulus (about 110 GPa) induces greater material springback of the machined surface, just behind the cutting edge, which increases tool flank wear and chatter, thus reducing the machinability [7].

The factors mentioned above are also affecting the surface integrity of machined Ti-6Al-4 V parts. Jawahir et al. [8] presented a comprehensive review on the experimental and modelling investigations on surface integrity induced by machining operations and its impact in the functional performance and life of components. They conducted an experimental round robin study to find correlations between the cutting conditions of several machining operations, the obtained surface integrity parameters (residual stresses, hardness, surface roughness), and the impact on the functional performance (in this case the wear resistance) of AISI 52,100 steel. Similar experimental study was performed by Denguir et al. [9] on the influence of several cutting parameters on the surface integrity (residual stresses, microstructure, plastic deformation and hardness), and electrochemical behaviour of machined OFHC Copper. As far as the surface integrity generated by machining of Ti-6Al-4 V titanium alloy is concerned, many experimental studies on the influence of the cutting conditions on this surface integrity can be found in the literature. Wang et al. [10] pointed out that the evolution of grain size and hardness of machined surface was dependent on the cutting speeds. During the end milling of Ti-6Al-4 V alloy, the milled surfaces characterized by surface roughness, residual stress, microstructure and microhardness were highly influenced by the feed, radial depth of cut and cutting speed [11]. Similarly, Holmberg et al. [12] and Pan et al. [13] investigated the effects of cutting speed, feed, tool rake angle and depth of cut on the surface roughness and residual stress in turning of Ti-6Al-4 V alloy. In order to improve the machinability and surface integrity, cooling/lubricant strategies, optimized cutting parameters and specially designed tool geometry/material were applied. Rotella and Umbrello [14] showed that high cutting speeds combined with cryogenic cooling with liquid nitrogen (LN₂) generated smaller grain size and higher hardness on the machined surface. Hong et al. [15, 16] achieved a decrease of cutting temperature, thus an increase of tool life in turning of Ti-6Al-4 V alloy using cryogenic cooling with LN₂. Ayed et al. [17] also obtained better tool life and an increase of compressive residual stress at the machined surface using high flow rate and high pressure of LN₂ compared to dry cutting and conventional MWF (oil–water mixture). Moreover, Jamil et al. [18] obtained the lowest value of the surface roughness in milling of Ti-6Al-4 V alloy under CO₂-snow cooling conditions, compared to conventional MWF and minimum quantity of lubricant (MQL).

The experimental studies presented above on the influence of cutting conditions on the surface integrity and their consequences on the functional performance and life of components

are quite relevant, but very time and resource consuming. Therefore, analytical models and numerical simulation are used to predict machinability and the surface integrity. Recently, artificial neural network (ANN), non-linear regression analysis and other artificial intelligence algorithms are increasing used to predict machining outcomes, such as the forces, temperatures and tool wear [19, 20]. The effectiveness of the numerical models to predict the machining outcomes depends on several factors. Outeiro et al. [21] presented the results of a benchmark study on the effectiveness of current numerical models for surface integrity prediction in metal cutting processes of several work materials, including the Ti-6Al-4 V titanium alloy. They observed a high variability in the simulated results obtained by several participants of this benchmark study and an important deviation in relation to the experimental data. To justify these results, they discussed several factors affecting the precision of the predicted results, which is related to the quality of the input data used in these simulations, including the material constitutive and contact models.

The contact model in metal cutting allows to describe the relationship between tangential and normal stresses at the tool-workpiece/chip interfaces. The contact along the tool-chip interface is often divided into two regions: plastic (near the tool cutting edge) and elastic (near the separation of the chip from the tool rake face). This is the case of the contact model of Zorev [22], often used in the metal cutting simulations, and of Dirikolu et al. [23]. These models require the determination of the friction coefficients under the same contact condition as those observed in metal cutting process. Courbon et al. [24] determined the friction coefficient between the Ti-6Al-4 V alloy and uncoated cemented carbide tools using a specially developed tribometre able to reproduce such contact conditions. In addition to the contact model, the selection of an appropriate model to reproduce the mechanical behaviour of the work material in metal cutting is also of primordial importance. These models can be classified into phenomenological, physical-based or the combination of both [25].

Chen et al. [26] and Zang et al. [27] used the phenomenological Johnson–Cook (J-C) constitutive model to study the effects of cutting conditions on the residual stress and chip geometry in orthogonal cutting of Ti-6Al-4 V alloy. To account for the flow softening effect due to the coupling condition of strain and temperature, the strain hardening term of J–C model was modified by integrating a Gaussian-like temperature dependent factor [28] or a hyperbolic-tangent (tanh) term [29]. The TANH model was also modified by several researchers to simulate the machining process [14] [30] [31]. Ducobu et al. [32] compared the influence of these constitutive models on the simulated results and demonstrated that both the material constitutive model and the chip separation criterion influenced cutting forces and chip

geometries. Instead of using the finite element method (FEM) method, Röthlin et al. [33] used smoothed particle hydrodynamics (SPH) method coupled with TANH model to simulate the orthogonal cutting of Ti-6Al-4 V alloy. Using the SPH method implemented in a graphics processing unit (GPU), they simulated the serrated chip formation typical of machining Ti-6Al-4 V alloy with a significant reduced computation time, compared to the same method implemented in a CPU. However, the thrust force is still largely underestimated. The underestimation of thrust force is often observed in metal cutting simulation, and it is not only inherent to meshless methods but also occurring when using also FEM method, as reported in many studies [14, 34].

Regarding the effect of the microstructural evolution in the mechanical behaviour, a physically-based constitutive model proposed by Fernandez-Zelaia et al. [35] was developed to describe the strengthening (e.g. dislocation interaction) and softening (e.g. dynamic recrystallization) of Ti-6Al-4 V. Although this model can better describe the mechanical behaviour in metal cutting compared to other phenomenological model such as J-C, it has limited use in metal cutting simulation due to the complexity and relatively numerous coefficients. Yameogo et al. [36] developed a hybrid constitutive model in the simulation of orthogonal cutting of Ti-6Al-4 V, which uses Johnson–Mehl–Avrami–Kolmogorov (JMAK) and J-C damage model to better simulate chip morphology when compared to the experimental chip morphology. Xu et al. [37] developed a multiscale simulation employing the TANH constitutive model, J-C damage model and JMAK model to investigate the grain refinement induced by DRX in high speed machining (HSM) of Ti-6Al-4 V titanium alloy. The microstructure evolution at mesoscopic level has been well predicted, and a more accurate model considering the effect of twinning and phase transformation was expected to be developed.

Since metal cutting is the plastic deformation of the work material until its separation from the workpiece to form the chip, the strain at fracture is an important property that should be considered. Unfortunately, this is not the case of most of the models mentioned above. Wang and Liu [38] modified J–C model to simulate the HSM of Ti-6Al-4 V alloy, and proved that the stress triaxiality played a vital role in serrated chip formation. Cheng et al. [39] also demonstrated the importance of the stress triaxiality and the Lode parameter in the improvement of constitutive model accuracy for predicting the mechanical behaviour of Ti-6Al-4 V alloy in metal cutting. It should be noted that the thermal softening term was not included in this model for two main reasons [39]. First, the mechanical tests at high strain rates already included the temperature effect. Second, the temperature in the first deformation zone (FDZ) hardly exceeds 200 °C due to mass transportation (i.e. heat advection) by the moving chip. Later, Xu et al. [40] extended the model

from Cheng et al. [39] and used the CEL approach to successfully simulate HSM of Ti-6Al-4 V alloy.

In this paper, an orthogonal cutting model of Ti-6Al-4 V alloy was developed and used to predict both cutting and thrust forces, chip geometry, chip compression ratio, temperature distribution in the cutting zone and residual stresses distributions in the machined surface and subsurface. The proposed orthogonal cutting model includes a constitutive model of the Ti-6Al-4 V alloy proposed by the authors in a previous publication [39]. This constitutive model includes the most relevant parameters affecting the mechanical behaviour (plasticity and damage) of Ti-6Al-4 V alloy in metal cutting (i.e. the state of stress and the strain-rate). It is worth to point out that the effect of state of stress (SoT) in the material plasticity and damage of Ti-6Al-4 V is almost not used in metal cutting simulation of this alloy (except the work of Xu et al. [40]), although it can significantly improve the mechanical response of the work material in cutting.

To evaluate the accuracy of the orthogonal cutting model including the proposed constitutive model considering the effect of the SoT, the predicted results using this model are compared with the experimental results (forces, chip geometry, chip compression ratio and residual stress distributions in function of the depth beneath the surface). To evaluate the effect of the SoT in the predicted results, the cutting force and chip geometry obtained by this cutting model are also compared with those obtained by a cutting model including the same constitutive model but neglecting the effect of the SoT, and those obtained by a cutting model including the J-C constitutive model.

A wide range of cutting conditions are used by varying several parameters (cutting speed, edge radius, rake angle, uncut chip thickness), thus a wide range of SoT in cutting of Ti-6Al-4 V alloy are generated and used to verify the accuracy of the developed orthogonal cutting model including the proposed constitutive model considering the effect of the SoT, to predict the major machining outcomes. It is also worth to point out that for most of the simulations shown in the literature this comparison is made only for a restrict number of cutting conditions

2 Experimental setup and cutting conditions

Ti-6Al-4 V titanium alloy used in this study is composed by two-phase structure ($\alpha + \beta$). The good balance between α and β phases makes it achieve high strength level without losing ductility [1]. Table 1 shows the chemical composition (weight percentage) of this alloy, obtained by rolling and annealing. Almost 90% of this alloy is composed by titanium, followed by 6% of aluminium, 4% of vanadium, 0.3% (max) of iron and 0.2% (max) of oxygen. The average

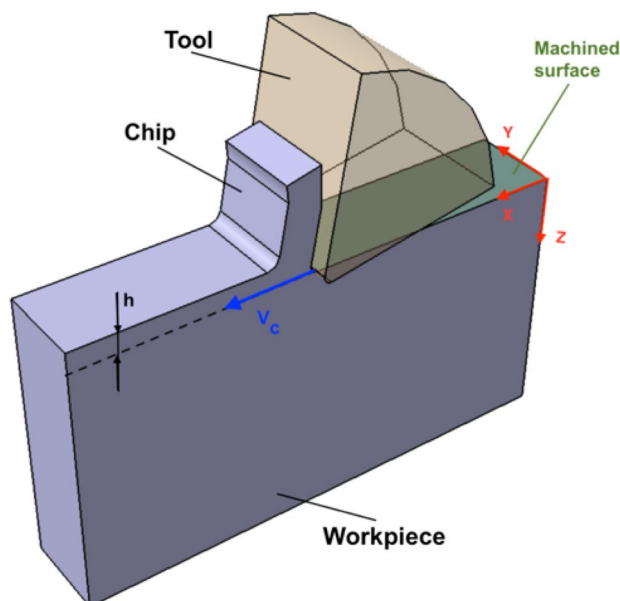
Table 1 Nominal chemical composition of Ti-6Al-4 V

Element	Al	V	Fe	O	C	N	Ti
Composition (wt%)	6.30	4.07	0.16	0.18	0.010	0.005	Remain

microhardness and grain size of this alloy are 330 ± 18 HV and 15.5 ± 1.8 μm , respectively.

Orthogonal cutting tests were performed over rectangular specimens (40 mm (sample/cutting length) \times 20 mm (sample height) \times 4 mm (sample width)) in Ti6Al4V alloy (Fig. 1) using uncoated cemented carbide (WC–Co) cutting tools. Tool geometry in the tool-in-hand system according to the ISO standard 3002:1982 was measured carefully using optical 3D measurement system, Alicona model InfiniteFocusSL. Each insert was placed in the holder to measure the tool rake, γ_n , tool clearance, α_n and cutting edge radius, r_n . These geometrical parameters were measured several times along each cutting edge, followed by the calculation of the average and standard deviation for each edge. Only the cutting edges having a geometry within a narrow range were used in the machining tests. The results of these measurements are shown in Table 2 together with the corresponding values of the cutting regime parameters (cutting speed V_c , uncut chip thickness h and width of cut w). All the tests were conducted under dry cutting conditions.

Orthogonal cutting tests in planning configuration are performed in a 3 axis CNC milling machine from DMG model DMC85V, as shown in Fig. 2. The tool was clamped in a square supporter which is fixed on the machine head. This milling machine has a linear motor to allow the linear speed to

**Fig. 1** Orthogonal cutting tests (X-longitudinal direction; Y-transversal direction)

reach up to 120 m/min and acceleration can reach 20 m/s^2 . A gradual acceleration has been performed by a speed loop-back command to reach the specified cutting speed in some millimetres before interaction between tool and workpiece. Each test was performed using a new cutting edge to eliminate the tool wear effect.

Cutting force F_c and thrust force F_T were measured by a piezoelectric dynamometer from Kistler, model 9119AA2, together with a charge amplifier Kistler, model 5019B.

During the orthogonal cutting tests, the chips were collected for further analysis. Chip's samples were prepared for metallographic analysis according to the standard ASTM E3-11 [41]. They were fixed into cylindrical resin sample holders under high temperature and pressure. Meanwhile, the chip was placed perpendicular to the base of the resin specimen, so the cross section of the chip could represent well the chip geometry. Then, this base was mirror polished. Finally, the polished samples were placed under the optical microscope to investigate the chip geometry. Three parameters were used to characterize its geometry: Peak, Pitch and Valley. Figure 3 shows the typical serrated chip morphology often observed in machining Ti6Al4V titanium alloy. Pitch corresponds to the distance between two adjacent peaks of the chip, the Peak and Valley represent the maximum and the minimum thicknesses of the chip, respectively. Each chip geometry parameter was measured 5 times for each cutting condition.

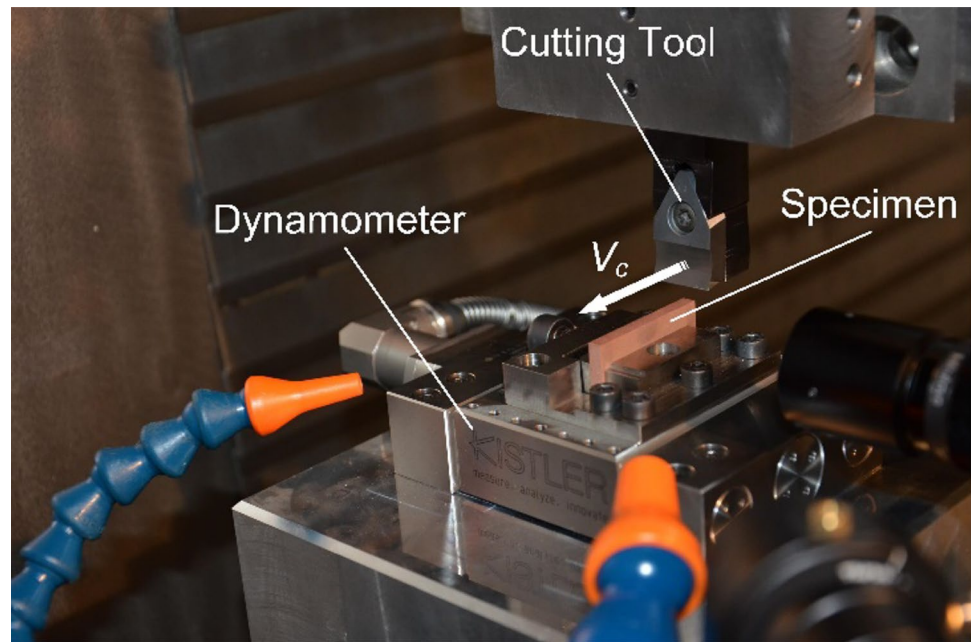
As mentioned by Astakhov and Shvets [42], CCR can be a measure of plastic deformation in metal cutting, since it does directly reflect the final plastic deformation that takes place in this process. CCR is the ratio between the chip thickness (h_1) and the uncut chip thickness (h), represented by Eq. (1),

$$CCR = \frac{h_1}{h} = \frac{V_c}{V_s} \quad (1)$$

where V_s is the chip speed (m/s). Since the chip thickness varies from a minimum (equal to the Valley) and a

Table 2 Cutting conditions used in orthogonal cutting test

Cutting parameters	Value
Cutting speed, V_c (m/min)	20; 60
Uncut chip thickness, h (mm)	0.15; 0.2
Tool cutting edge radius, r_n (μm)	16 ± 1.1 ; 30 ± 1.9
Tool rake angle, γ_n ($^\circ$)	5 ± 0.13 ; -6 ± 0.25
Tool clearance angle, α_n ($^\circ$)	6 ± 0.23
Width of cut, w (mm)	4
Cooling condition	Dry cutting

Fig. 2 Experimental setup

maximum value (equal to the Peak), three CCR values can be calculated for each cutting condition: a minimum (CCR_{min}), a maximum (CCR_{max}) and an average (CCR_{aver}).

Finally, residual stresses were measured at the machined surface and subsurface of the samples using the X-ray diffraction technique in the longitudinal (x-direction in Fig. 1) and transversal (y-direction in Fig. 1) directions using Seifert XRD 3000 PTS equipment. Measurements were made with the diffraction of copper K- α radiation from the {213} crystallographic plane of the Ti6Al4V alloy. Diffractograms were recorded for 29 tilt angles ψ varying between -45° and $+45^\circ$. To calculate the residual stress, the $\sin^2\psi$ method was used [43]. The X-ray elasticity constants $1/2 S_2$ and S_1 providing the proportionality between measured strains and calculated stresses have been calculated owing to an elastic self-consistent model: $1/2 S_2 = 11.68 \times 10^{-6} \text{ MPa}^{-1}$, $S_1 = -2.83 \times 10^{-6} \text{ MPa}^{-1}$. Measurements were performed in the centre of the machined surface. The irradiation zone had a length of 4 mm and width 2 mm. The penetration depth of the X-ray radiation was about 5 μm . To measure the residual stress beneath the surface, the layers were successively

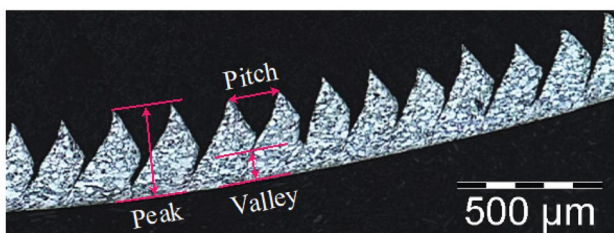
removed by electrolytic polishing method using Presi Poliseq C20 equipment to avoid reintroducing additional residual stresses.

3 Orthogonal cutting model

3.1 General description

2D orthogonal cutting model of Ti-6Al-4 V titanium alloy is developed and simulated using the Lagrangian approach in ABAQUS/Explicit FEA software. This model and corresponding boundary conditions are shown in Fig. 4. It is composed by the workpiece (1) and tool (2). The workpiece is divided into three layers or parts: upper layer used to form the chip (1a), intermediate layer (1b) and bottom layer that corresponds to the machined workpiece (1c). The intermediate layer is applied to simulate the physical separation of the layer being removed (in the form of chips) from the rest of the workpiece, using the element deletion technique. The workpiece is fixed in the bottom in both X and Y directions, while the tool is moving along the negative X-direction at a speed equal to the cutting speed (V_c) and fixed in the Y-direction. The bottom and right sides of the workpiece together with the right and upper sides of the tool are at room temperature of 20 $^\circ\text{C}$. To simulate the dry cutting conditions, the other sides of the workpiece and tool are convective surfaces with the air, with a coefficient of heat convection of 23 $\text{W}/\text{m}^2/^\circ\text{C}$ [44]. An initial temperature of 20 $^\circ\text{C}$ is imposed to both the tool and the workpiece.

The quadrilateral continuum elements CPE4RT are used. Refined elements are used in the parts of chip and

**Fig. 3** Chip geometry parameters measured by optical microscope

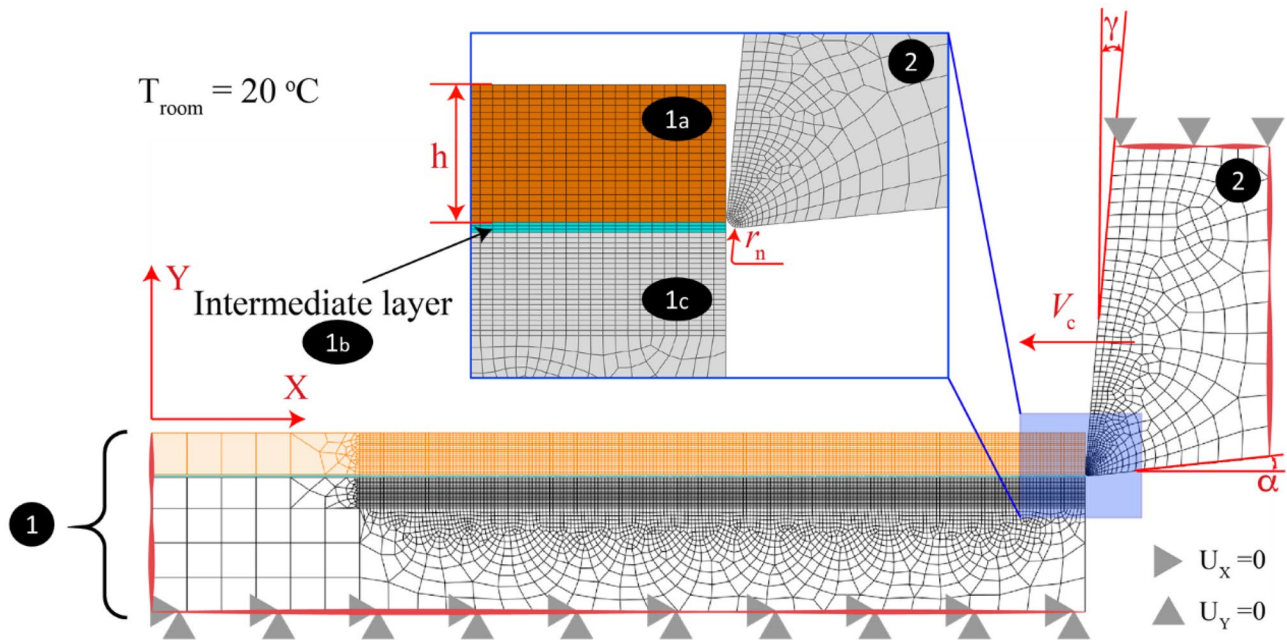


Fig. 4 2D orthogonal cutting model

intermediate layer to better simulate the cutting process, where the mesh size is $17 \mu\text{m} \times 10 \mu\text{m}$. Meanwhile, the mesh along the depth of workpiece surface is also refined to calculate the distribution of residual stress, where the mesh size was defined as $17 \mu\text{m} \times 7.5 \mu\text{m}$.

A coupled thermo-mechanical analysis was performed. The elastic and thermal properties of the of Ti-6Al-4 V titanium alloy and of the cutting tool are given in Table 3. Thermal properties of Ti-6Al-4 V alloy are provided by the titanium supplier, while information of the tool material is taken from the literature [21].

3.2 Material constitutive model

As far as the constitutive model of Ti-6Al-4 V alloy is concerned, the model proposed by Cheng et al. [39] is used, which includes both plasticity and damage formulations that were

implemented in Abaqus through VUMAT and UMAT subroutines. The plasticity model incorporates the strain hardening, strain rate and SoT effects, and shown from Eqs. (2)–(4).

$$\tilde{\sigma} = \left(A + m\epsilon_p^n \right) \left[B + C \ln \left(E + \frac{\dot{\epsilon}}{\dot{\epsilon}_0} \right) \right] \left[1 - c_\eta (\eta - \eta_0) \right] \left[c_\theta^S + (c_\theta^{ax} - c_\theta^S) \left(\gamma - \frac{\gamma^{a+1}}{a+1} \right) \right] \quad (2)$$

$$\gamma = 6.464 \left[\sec \left(\frac{\bar{\theta}\pi}{6} \right) - 1 \right] \quad (3)$$

$$c_\theta^{ax} = \begin{cases} c_\theta^t & \text{for } \bar{\theta} > 0 \\ c_\theta^c & \text{for } \bar{\theta} \leq 0 \end{cases} \quad (4)$$

In the previous equations: (i) the coefficients A , m and n are used in the strain hardening term; (ii) the coefficients B , C and E are used in the strain rate term; (iii) the coefficient c_η is used in the stress triaxiality term; (iv) the coefficients $c_\theta^t, c_\theta^c, c_\theta^s$ and a are used in the Lode parameter term; (v) η_0 is the reference stress triaxiality and $\dot{\epsilon}_0$ is the reference strain rate; (vi) γ describes the difference between Tresca and von-Mises equivalent stresses on the deviatoric stress plane, and given by Eq. (3); and (vii) the coefficients $c_\theta^t, c_\theta^c, c_\theta^s$ are interdependent and at least one of them is equal to 1. Considering the compression test of cylindrical specimen at quasi-static conditions as a reference, η_0 is equal to $-1/3$, $\dot{\epsilon}_0$ is equal to 0.05 s^{-1} and c_θ^c is equal to 1. The temperature effect on the work material behaviour is not considered in this plasticity

Table 3 Thermal and physical properties of the workpiece and the tool

Physical properties	Workpiece	Tool
Density, ρ (kg/m ³)	4420	13,967
Elastic modulus, E (GPa)	114	627.5
Poisson's ration, ν	0.31	0.25
Specific heat, C_p (J/kg $^\circ\text{C}$)	670	100
Thermal conductivity, λ (W/m $^\circ\text{C}$)	6.6	9.7
Coefficient of thermal expansion, α_v ($\mu\text{m}/\text{m}^\circ\text{C}$)	9	5.174

Table 4 Coefficients of the plasticity model [39]

	Strain hardening			Strain rate			Reference	
Coefficient	<i>A</i>	<i>m</i>	<i>n</i>	<i>B</i>	<i>C</i>	<i>E</i>	$\dot{\epsilon}_0$	η_0
Value	812.1	625.7	0.176	0.400	0.073	3949	0.05	− 1/3
	Stress triaxiality			Lode angle				
Coefficient	c_η			c_θ^s	c_θ^l		c_θ^c	<i>a</i>
Value	0.212			0.795	1.061		1	4

model for the main reasons already mentioned in the ‘‘Introduction’’ [39].

The damage model includes damage initiation and damage evolution, as shown from Eqs. (5)–(7). Equation (5) represents the damage initiation, while Eqs. (6) and (7) represent the damage evolution.

$$\bar{\epsilon}_i^p = \left\{ \left[\frac{1}{2} (D_1 e^{-D_2 \eta} + D_5 e^{-D_6 \eta}) - D_3 e^{-D_4 \eta} \right] \bar{\theta}^2 + \frac{1}{2} (D_1 e^{-D_2 \eta} - D_5 e^{-D_6 \eta}) \bar{\theta} + D_3 e^{-D_4 \eta} \right\} \times \left[1 + D_7 \ln \left(\frac{\dot{\epsilon}}{\dot{\epsilon}_0} \right) \right] \tag{5}$$

$$\bar{\sigma} = (1 - D) \tilde{\sigma}, D = \frac{1 - \exp(\lambda \epsilon^*)}{1 - \exp(\lambda)}, \epsilon^* = \frac{\bar{\epsilon}^p - \bar{\epsilon}_i^p}{\bar{\epsilon}_f^p - \bar{\epsilon}_i^p} \tag{6}$$

$$G_f = \int_{\bar{\epsilon}_i^p}^{\bar{\epsilon}_f^p} l \bar{\sigma} d\bar{\epsilon}^p = \int_0^{\bar{\mu}_f} \bar{\sigma} d\bar{u} \tag{7}$$

In these equations, D_1 – D_7 are the coefficients of damage initiation, where D_1 – D_6 are affecting the SoT, and D_7 is affecting the strain rate. λ controls the material degradation rate, and G_f is the material fracture energy density; $\bar{\epsilon}_i^p$ is the plastic strain at damage initiation; $\bar{\epsilon}_f^p$ is the plastic strain when all the stiffness and the fracture energy of the material have been lost and dissipated; $\tilde{\sigma}$ is the hypothetical undamaged stress evaluated by Eq. (2); l is the characteristic length of the finite element; $\bar{\mu} = 0$ relates to the equivalent plastic displacement before damage initiates; and $\bar{\mu}_f$ is the equivalent plastic displacement at complete fracture. An inverse approach based on an optimization-based algorithm was used to determine the coefficients of the constitutive model, which consists into simulating the mechanical tests, by modifying the coefficients iteratively, to minimize the difference between the predicted and measured force–displacement curves. A detailed description of this approach can be found in a previous publication of the authors [45], and the values

of these coefficients are given in Tables 4 and 5. In the case of the damage evolution, G_f and λ are equal to 18.5 kJ/m² and 9.4, respectively [39].

However, to evaluate the effect of the SoT in the predicted cutting results the J – C model without the thermal softening term is also used. This constitutive model also includes both plasticity and damage formulations given by Eqs. (8)–(9).

$$\tilde{\sigma} = \left(A_{jc} + B_{jc} \epsilon_p^{n_{jc}} \right) \left[1 + C_{jc} \ln \left(\frac{\dot{\epsilon}}{\dot{\epsilon}_0} \right) \right] \tag{8}$$

$$\bar{\epsilon}_i = (D_{1jc} + D_{2jc} e^{D_{3jc} \eta}) \left[1 + D_{4jc} \ln \left(\frac{\dot{\epsilon}}{\dot{\epsilon}_0} \right) \right] \tag{9}$$

$$D = 1 - \exp \left(- \int_0^{\bar{u}} \frac{\bar{\sigma}_y}{G_f} d\bar{u} \right); G_f = \int_{\bar{\epsilon}_i^p}^{\bar{\epsilon}_f^p} l \bar{\sigma}_y d\bar{\epsilon} = \int_0^{\bar{\mu}_f} \bar{\sigma}_y d\bar{u} \tag{10}$$

$$\bar{\sigma} = (1 - D) \tilde{\sigma} \tag{11}$$

A_{jc} , B_{jc} , C_{jc} and n_{jc} are the coefficients of the plasticity model, and $\dot{\epsilon}_0$ is the reference strain rate which equals 0.05 s^{−1}. D_{1jc} – D_{4jc} are the damage coefficients, and G_f is the fracture energy density. $\bar{\epsilon}_i$ is the plastic strain at damage initiation, and $\bar{\epsilon}_f$ is the plastic strain when all the stiffness and fracture energy of the material have been lost and dissipated, respectively. As described by Cheng et al. [39], the coefficients of the J – C model were determined using the mechanical test data which had been also applied to determine the above-mentioned proposed model. Due to the simplicity of J – C model, the coefficients in the plasticity model and the damage model coefficient related to the strain rate effect (D_{4jc}) were determined by the compression tests of cylindrical specimens, while the compression tests of double notched specimens were used to determine the damage model coefficients associated with the stress triaxiality effect (D_{1jc} – D_{3jc}). The value of G_f is the same of the proposed

Table 5 Coefficients of the damage initiation model [39]

Damage coefficients	D_1	D_2	D_3	D_4	D_5	D_6	D_7
	0.694	0.608	0.263	0.734	0.430	0.040	−0.028

Table 6 Determined coefficients of the J–C model [39]

Coef	Plasticity				Damage				G_f (KJ/m ²)	$\dot{\epsilon}_0$ (s ⁻¹)
	A_{jc}	B_{jc}	n_{jc}	C_{jc}	D_{1jc}	D_{2jc}	D_{3jc}	D_{4jc}		
Value	812	844	0.261	0.015	0.245	0.081	-1.276	-0.028	18.5	0.05

model. Table 6 presented the determined coefficients of the J–C constitutive model for the Ti6Al4V alloy [39].

3.3 Contact model

Zorev’s model [46] is adopted in this work to describe the contact stresses at tool-workpiece interface. Mathematically, this model can be represented by Eq. (12).

$$\tau = \begin{cases} \mu \cdot \sigma & \text{if } \mu \cdot \sigma < \tau_{lim} \\ \tau_{lim} & \text{if } \mu \cdot \sigma \geq \tau_{lim} \end{cases} \quad (12)$$

where σ and τ are the normal and shear stresses, and μ is the friction coefficient at the interface. Therefore, for sliding contact conditions at the interface ($\mu\sigma < \tau_{lim}$), the shear stress will be calculated using the Coulomb friction model ($\tau = \mu\sigma$), while for plastic contact conditions at the interface ($\mu\sigma \geq \tau_{lim}$), the sliding does not occur at the tool-chip interface but in the adjacent layers of the chip, being the shear stress equal to the shear stress limit, τ_{lim} . This shear stress limit can be determined by $\sigma_y/\sqrt{3}$, where σ_y is the yield stress of the workpiece and chip materials, which is calculated during the simulation of the machining.

The value of the friction coefficients between the Ti6Al4V and the uncoated tungsten carbide should be determined by tribological tests under identical contact conditions as those applied during machining, concerning to sliding speed, pressure, temperature, lubrication, etc.

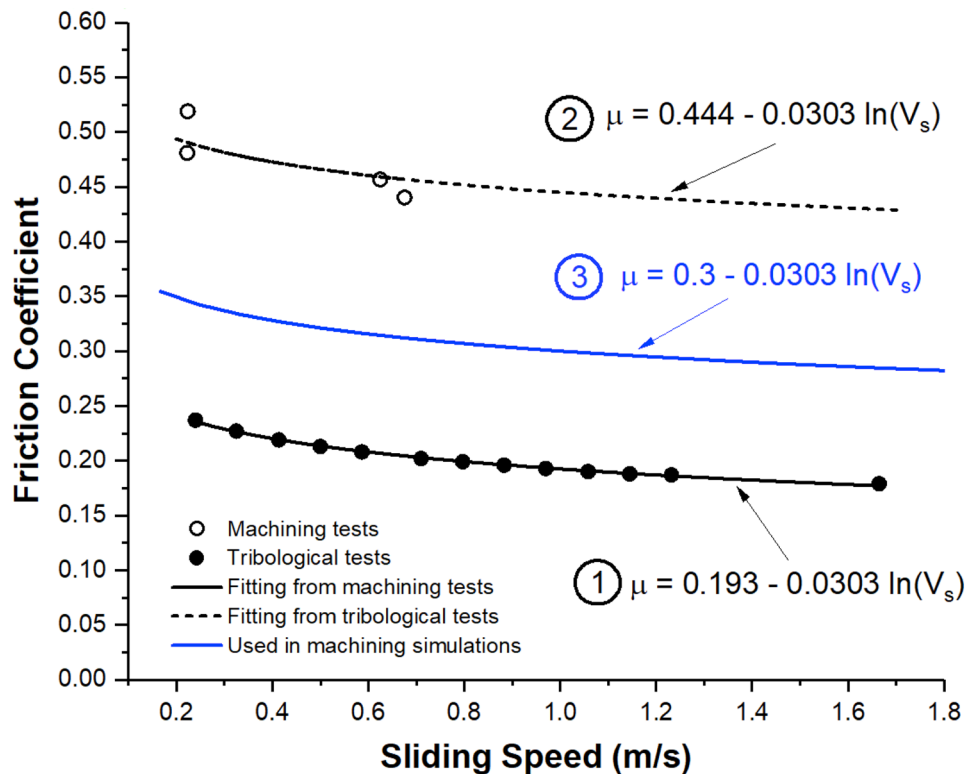
Courbon et al. [24] performed tribological tests using a special device able to generate the contact conditions close to those found in machining. They determined the friction coefficient as a function of sliding speed, as shown by curve 1 in Fig. 5 and given by Eq. (13).

$$\mu = a + b \ln V_s \quad (13)$$

where a and b are constants. However, the friction coefficients were also determined through the orthogonal cutting tests over Ti-6Al-4 V alloy using uncoated tungsten carbide cutting tools under 4 selected sets of cutting regime parameters. The friction coefficient was calculated by Eq. (14),

$$\mu = \frac{F}{N} = \frac{F_t + F_c \tan \gamma}{F_c + F_t \tan \gamma} \quad (14)$$

Fig. 5 Friction coefficient in function of the sliding speed between Ti-6Al-4 V alloy and uncoated tungsten carbide. Friction coefficient determined by tribological [24] (curve 1) and orthogonal cutting (curve 2) tests, and used in the orthogonal cutting simulations (curve 3)



where F and N are the tangential and normal forces to the tool rake face, respectively. These forces are calculated based on the measured cutting (F_c) and thrust (F_t) forces. The obtained friction coefficients are given by *curve 2* in Fig. 5, assuming that the slope is the same of *curve 1*. This assumption is because both machining and tribological tests are conducted for the same workpiece and tool materials, the same lubrication/cooling conditions and the same range of sliding speeds.

Astakhov and Outeiro [47] have shown that the friction coefficient is often overestimated when calculated using the forces from orthogonal cutting tests. Moreover, the friction coefficient depends on the sliding speed but also on the contact temperature and contact pressure. The accurate determination of the contact conditions in metal cutting is a challenging task. In most of the cases these conditions are roughly estimated based on temperature measurements inside the tool, which do not represent the temperature at the tool-chip and tool-workpiece interface. Moreover, the contact pressure is also roughly estimated based on the measurements of the forces and tool-chip contact length in orthogonal cutting. Performing tribological tests using contact conditions roughly estimated will result in an incorrect determination of the friction coefficient. Therefore, the true friction coefficients for given tool-work material pair and contact conditions will be different from those estimated using tribological tests (*curve 1*) and machining data (*curve 2*).

After running several simulations for both friction curves (1 and 2) and for 5 different cutting speeds, covering the range of speeds shown in Fig. 5, non-negligible differences between measured and predicted forces and chip geometry are found. Considering that this difference is due to the friction coefficient, a calibration procedure was applied by varying the coefficient a of the friction equation (Eq. (13)) until the predicted forces and chip geometry are close enough to those measured.

Curve 3 in Fig. 5 represents the friction curve that provided the lowest difference between simulated and measured forces and chip geometry. As shown in this figure, the friction coefficients to be used in the orthogonal cutting simulations (*curve 3*) are between *curve 1* (lower limit) and *curve 2* (upper limit).

3.4 Residual stresses calculation and extraction from the model

The model to predict the residual stress was developed and simulated using Lagrangian approach in ABAQUS/Standard (implicit method) FEA software. After the orthogonal cutting simulation was performed using ABAQUS/Explicit, the machined workpiece and the associated thermo-mechanical fields (part 2c in Fig. 4) are transferred to ABAQUS/Standard for residual stress calculation. This calculation consists into unloading and cooling of the workpiece until reaching the mechanical equilibrium and room temperature, respectively.

The constitutive model used in residual stress calculation is the same of the cutting simulation, and it was implemented in ABAQUS/Standard using a UMAT subroutine. The initial state of the model for the residual stress calculation is obtained from the last step of the cutting model. After residual stress calculation, their values in function of the depth beneath surface are extracted using the procedure described by Outeiro [48].

4 Comparison between measured and simulated results

4.1 Forces, chip geometry and chip compression ratio

Figure 6 shows an example of the comparison between simulated and measured forces, chip geometry and maximum chip compression ratio (CCR_{max}) for $\gamma = 5^\circ$, $r_n = 16 \mu\text{m}$, $V_c = 20 \text{ m/min}$ and $h = 0.15 \text{ mm}$. Figure 6a presents the von-Mises stress distribution in the workpiece and chip. This figure shows a chip segmentation typical of machining Ti-based alloys. The simulated shape of the chip segments is very close to those observed experimentally (also shown in Fig. 6a). Moreover, Fig. 6a shows a maximum stress value in the FDZ, that can reach about 1700 MPa. This maximum stress and the size of the region of high stresses in the workpiece ahead of the cutting tool vary cyclically during the cutting process. This is due to the cyclic nature of the chip formation process, which is characteristic to machining Ti-based alloys.

Figure 6b. shows a comparison between experimental and simulated chip geometry and CCR_{max} . The value of the chip peak obtained in the experiments is close to the simulated one, which is also the case for the CCR_{max} value. However, the simulated values of the chip valley and pitch are slightly higher than those measured experimentally.

The simulated cutting and thrust forces are shown in Fig. 6c. When compared to the experimental forces, the simulated cutting force is relatively well predicted, while the simulated thrust force is largely underestimated. There are three main reasons for the underestimated thrust force. First, to avoid excessive mesh distortion, the initial position of the tool is not in direct contact with the top surface of machined workpiece (layer 1c in Fig. 4) or the machined surface, but slightly above this surface. During cutting, the deformation of the workpiece ahead the cutting edge brings its top surface in contact with the flank face of the tool, but the contact conditions are not representative of the real tool-workpiece contact. The second reason is related to the Zorev's contact model given by Eq. (12), which in the present study is used to represent both tool-chip and tool-workpiece contacts. The so-called Zorev's contact model

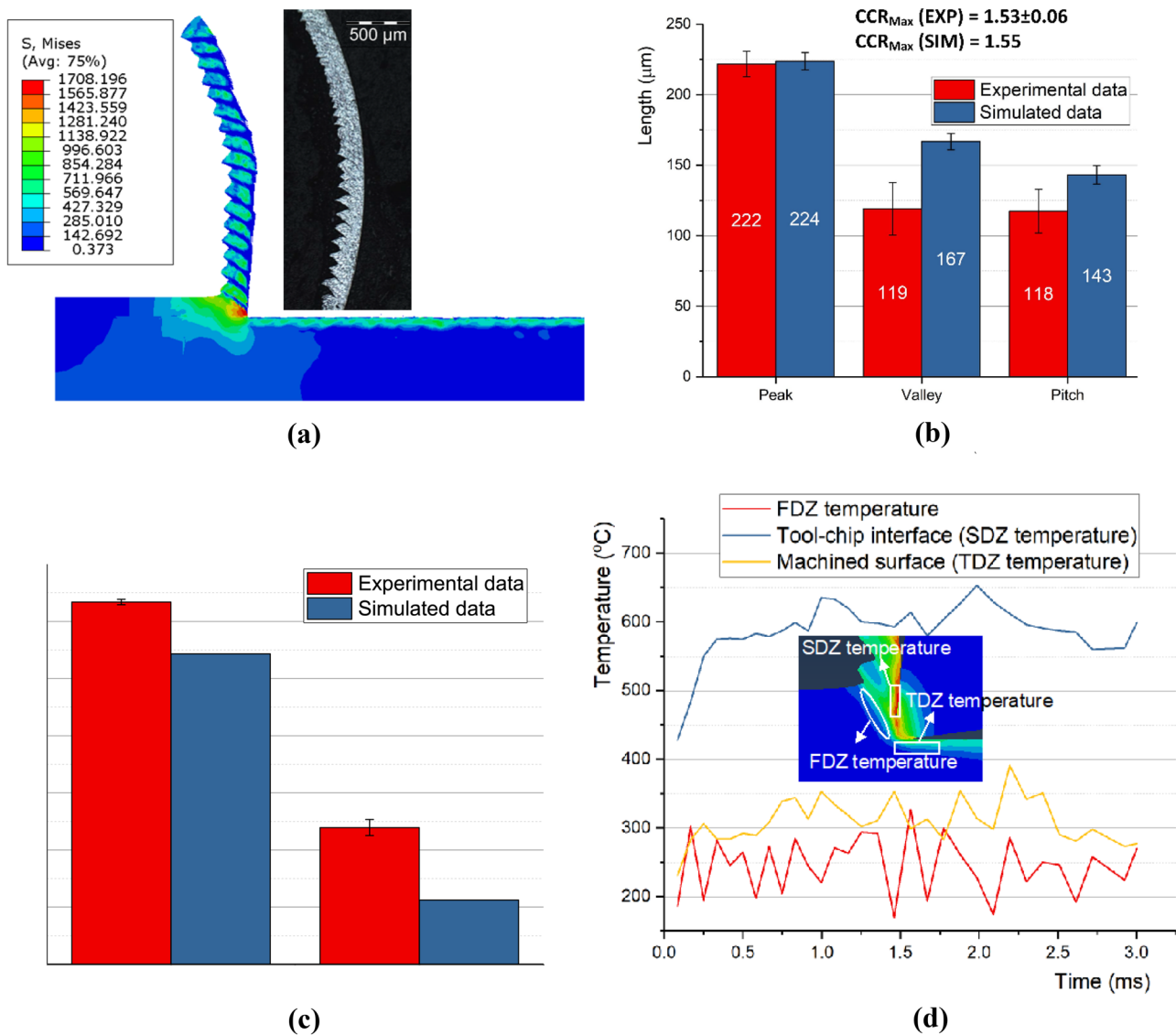


Fig. 6 Simulated and experimental results of orthogonal cutting ($\gamma=5^\circ$, $V_c=20$ m/min, $h=0.15$ mm, $r_n=16$ μm): **a** von-Mises stress distribution, **b** chip geometry and CCR_{max} , **c** forces, **d** temperatures

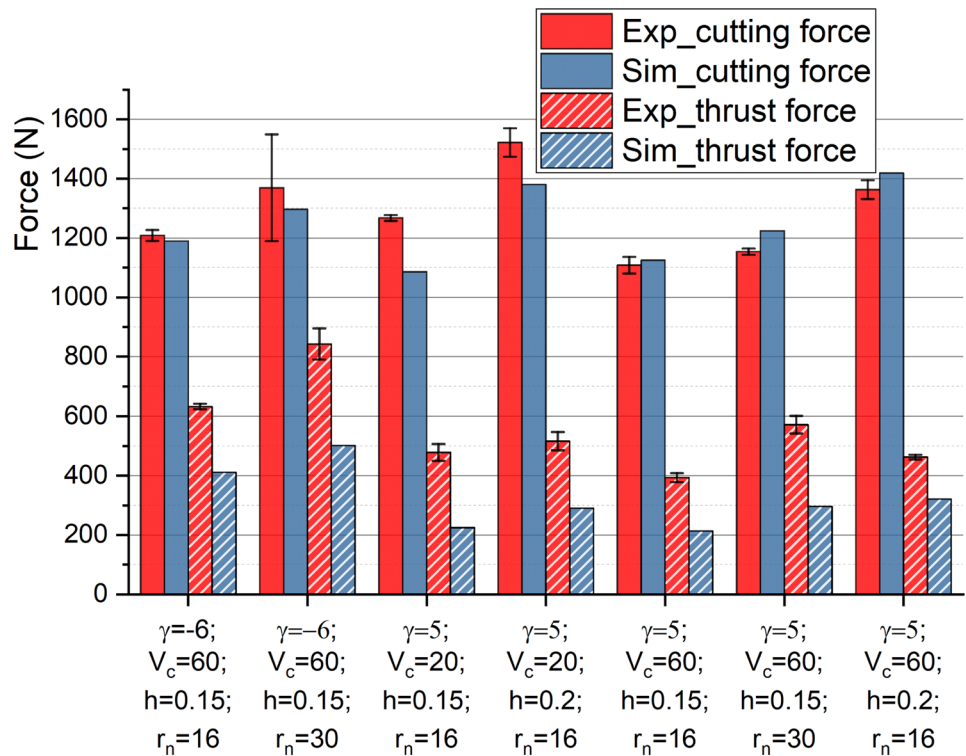
can reasonably estimate the contact stresses at tool-chip, but according to Astakhov [49] is not suitable to estimate the contact stresses at tool-workpiece interface. Finally, the third reason is the great springback of the titanium alloy, which are not correctly modelled, and can substantially affect the tool-workpiece contact.

Figure 6d shows the predicted temperatures during the cutting simulation, including the cutting temperature (maximum integral temperature at the tool-chip interface), the maximum temperature in the FDZ and the maximum temperature in the third deformation zone (TDZ). The cutting temperature increases rapidly to 600 °C in less than 1 ms before reaching a stable value, while the temperature in FDZ varies almost cyclically around 220 °C, putting in evidence

the influence of the cyclic nature of chip formation in this temperature. The temperature in the FDZ is not enough to influence the mechanical behaviour of the work material. The temperature in the TDZ stays around 300 °C.

For the other cutting conditions, the simulated results are also compared with the experimental ones, including the chip geometry, cutting and thrust forces. Figure 7 shows the comparison between experimental and simulated cutting and thrust forces for seven cutting conditions. Like Fig. 6, the cutting force is well predicted where the differences between measured and predicted values are less than 14%, but this is not the case of the thrust force, where the maximum difference can reach 53%.

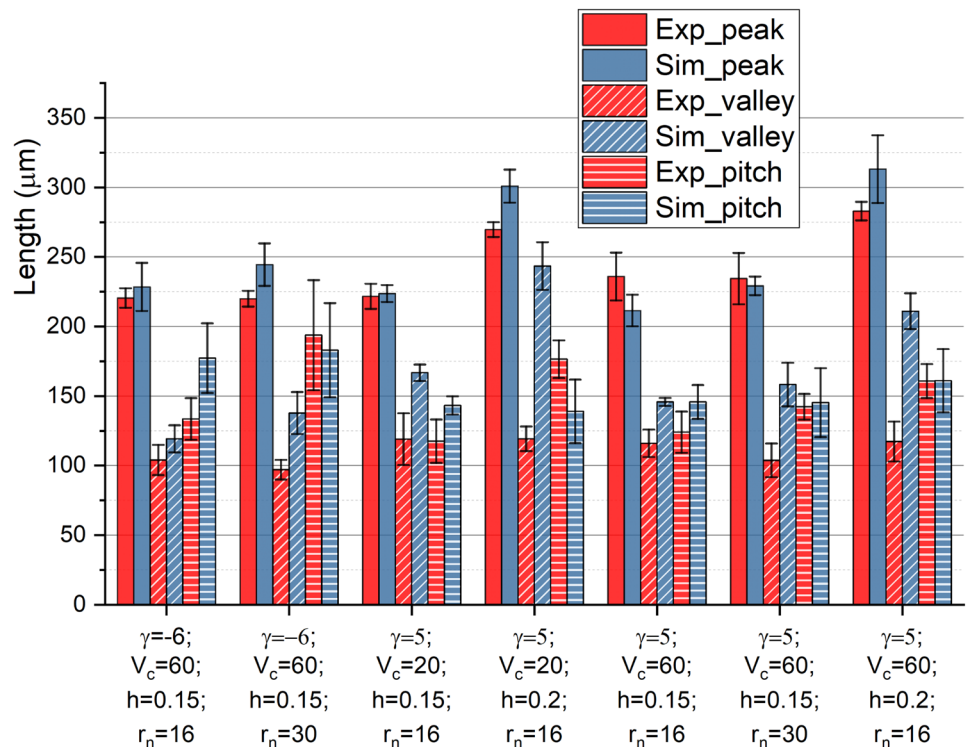
Fig. 7 Comparison between the simulated and experimental forces



As far as the chip geometry is concerned, Fig. 8 shows that the peak and pitch parameters are also well predicted, but small differences between experimental and simulated values of the chip valley are observed.

In particular, the average differences for chip peak and pitch are only 7% and 14% respectively, while the average difference for chip valley is 51%. These differences are also found in the literature for the simulation of

Fig. 8 Comparison between simulated and experimental chip geometry



the orthogonal cutting of Ti-6Al-4 V alloy [36, 44, 50]. According to Chen et al. [50], it is caused by the crack formation and propagation at the adiabatic shear bands near the chip free surface, which are not reproduced using the numerical method used in the present study.

As far as CCR_{max} is concerned, Fig. 9 compares the simulated values of this parameter with those obtained experimentally. As can be seen, CCR_{max} is varying from about 1.3 to 1.6, which agree to those values of this parameter obtained by other researchers [21, 51, 52]. In general, the CCR_{max} is quite well predicted by the numerical simulations when comparing both simulated and experimental values of this parameter. The average difference between predicted and measured CCR_{max} does not exceed 10%.

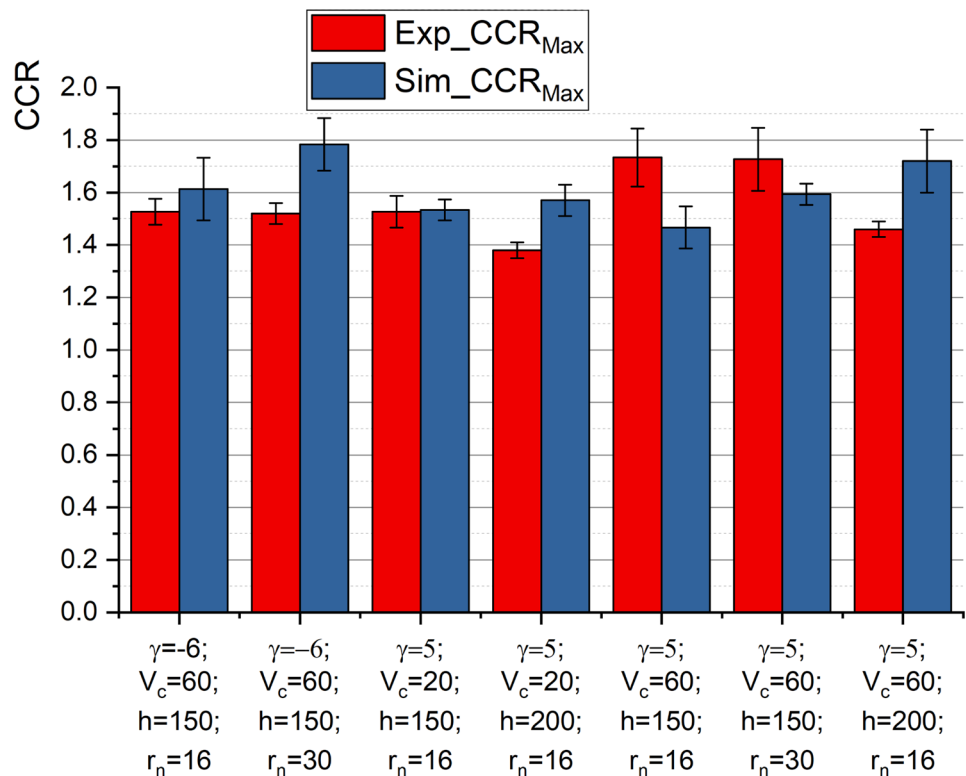
Cheng et al. [39] have shown that a constitutive model considering the SoT significantly improves the prediction of the mechanical behaviour of Ti6Al4V titanium alloy for a wide range of loading conditions. Since the change of cutting conditions induces different SoT [53], this constitutive model should improve the predictability of the machining model when compared to other constitutive models neglecting the SoT. To verify this, the cutting force and chip geometry predicted by this cutting model were compared with the cutting force and chip geometry predicted by other two cutting models: one including the proposed constitutive model of Cheng et al. [39] without considering the SoT, and another including the $J-C$ model. As shown

in Fig. 10a, the proposed constitutive model considering the SoT predicts quite well the cutting force (maximum difference can reach 5%), while the predicted cutting forces using the proposed constitutive model without considering the SoT or the $J-C$ model can be significantly different from the measured one (maximum difference can reach 22%). As far as the chip geometry is concerned, Fig. 10b shows that in general the proposed constitutive model considering the SoT predicts better the chip geometry than the $J-C$ model.

4.2 Residual stresses in the machined surface and subsurface

Figure 11 shows the schematic representation of the typical in-depth residual stress profiles in both longitudinal and transversal directions after machining Ti-6Al-4 V alloy. Residual stresses at the machined surface are often compressive or low tensile. The level of residual stresses in both directions changes continuously with depth down to a certain maximum value below the surface for most of the cutting conditions, and then gradually decreases stabilizing at the level corresponding to that found in the work material before machining. The actual depth at which the circumferential residual stresses reach the zero-stress value can be thought of as the thickness of the layer affected by residual stresses due to machining.

Fig. 9 Comparison between simulated and experimental CCR_{max}



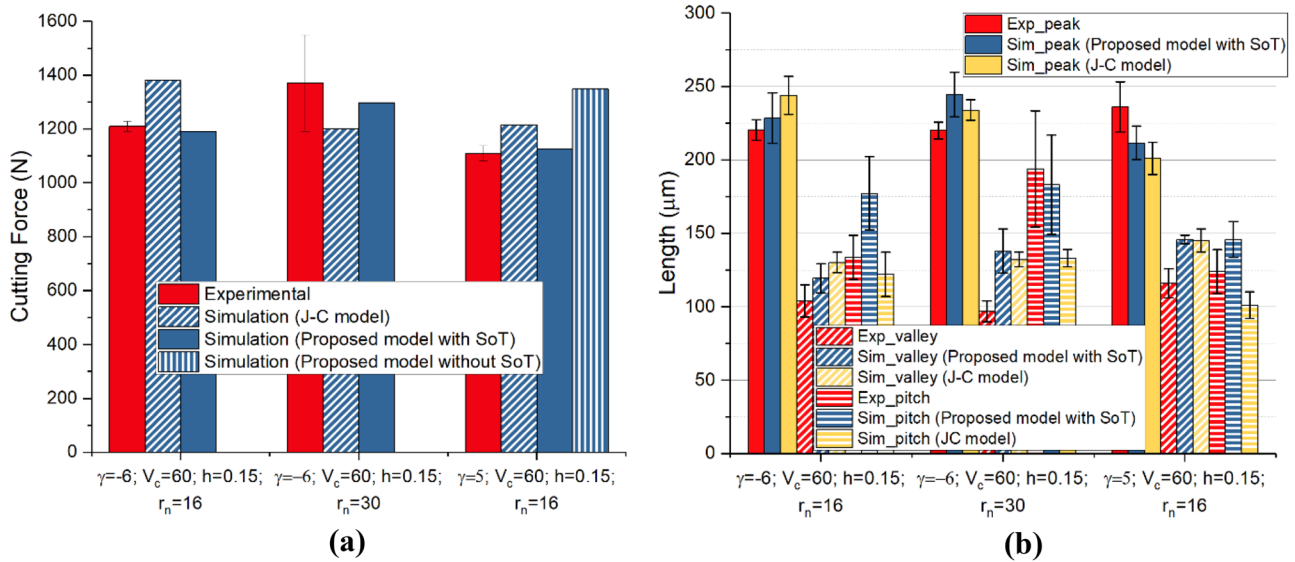


Fig. 10 Comparison between experimental results and those predicted using the proposed constitutive model (with and without the SoT) and the Johnson–Cook model: **a** cutting force; **b** chip geometry

As shown in Fig. 11, several parameters are used to characterize the in-depth residual stress profiles:

- residual stress at the machined surface (*SRS*);
- maximum residual stress in compression beneath the surface (*MRS*);
- depth where the maximum compressive stress is located (*Depth_MRS*);
- thickness of the layer affected by residual stresses due to machining (*Layer_RS*).

Figure 12 shows both measured in-depth residual stress profiles determined experimentally by XRD technique,

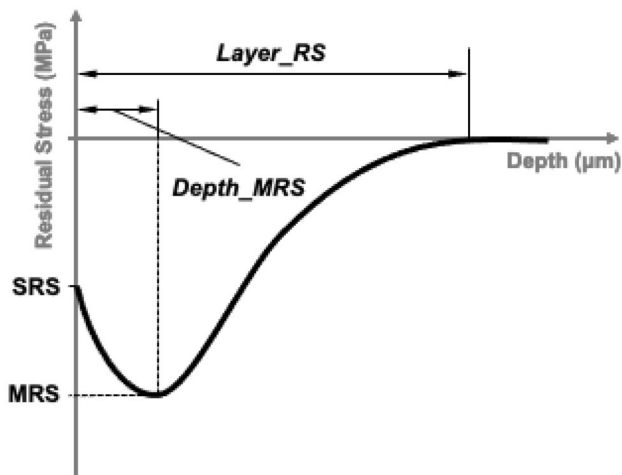


Fig. 11 Schematic representation of the typical in-depth residual stress profile

and those stress profiles simulated using the orthogonal cutting model for the seven selected cutting conditions. Experimentally, for all the cutting conditions, the residual stress in the longitudinal direction is more compressive than the stress in the transversal direction. At the machined surface, the residual stress in longitudinal direction is always high compressive for all the cutting conditions, reaching about -600 MPa, whereas in the transversal direction both low compressive and low tensile stresses can be found.

The level of residual stress in the transversal direction changes continuously with depth down to a certain maximum value below surface, reaching -400 MPa (*MRS*) between 20 and 40 μm below the surface (*Depth_MRS*). Then, it gradually decreases stabilizing around zero. This kind of in-depth residual stress profile can also be found in the longitudinal direction, except for the cutting condition indicated in Fig. 12a, where the *MRS* is shifted the machined surface. The thickness of the layer affected by residual stresses due to machining (*Layer_RS*) varies from 110 to 150 μm depending on the cutting conditions.

Figure 12 also shows some differences between the measured and simulated in-depth residual stress profiles. The biggest differences are observed for the following two cases:

- Between the measured and predicted longitudinal stresses until about 20 μm below the surface (hereby called near surface residual stresses) for all the seven cutting conditions. In this case, the predicted residual stresses in longitudinal direction are much lower in compression than the measured ones.

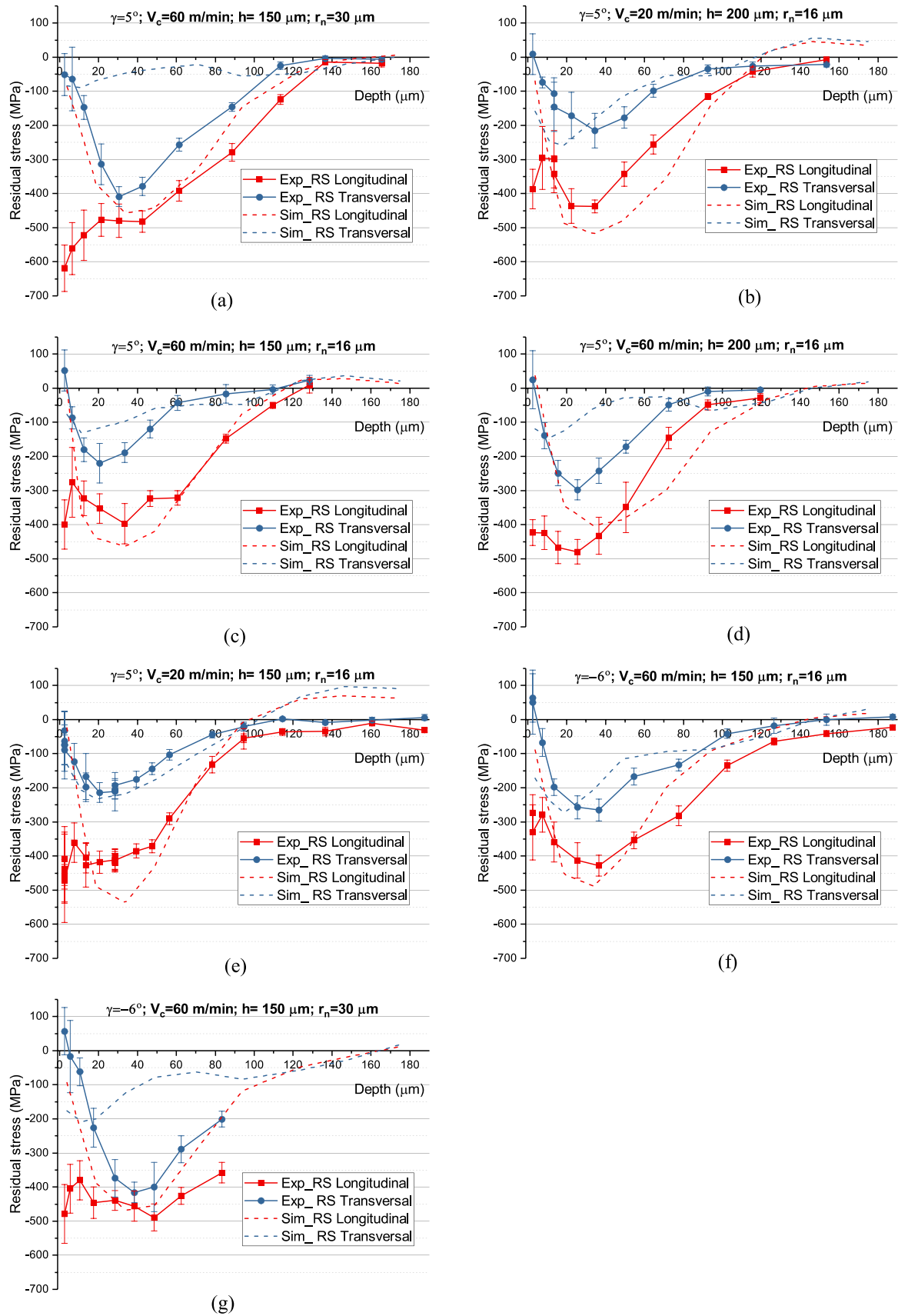
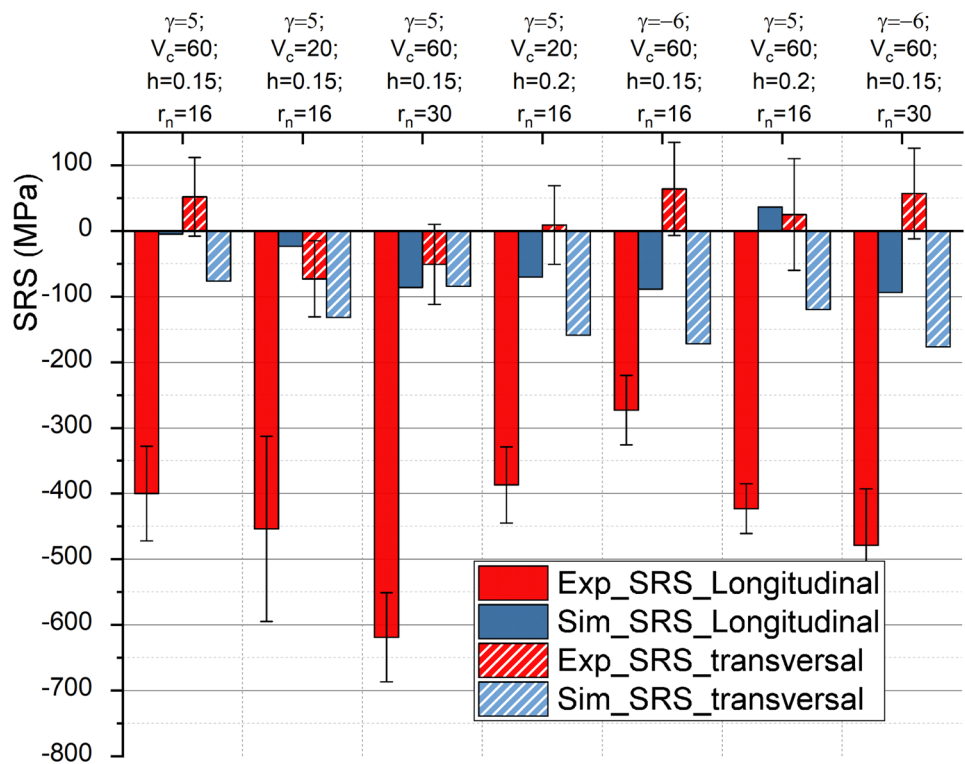


Fig. 12 Comparison between simulated and experimental distribution of residual stress

Fig. 13 Simulated and measured residual stresses at machined surface (SRS)



- Between the measured and predicted transversal stresses after about 20 μm below the surface for three cutting conditions indicated in Fig. 12a, d and g.

Except for these two cases, the predicted residual stresses are very close to those measured. In particular:

- The predicted near surface residual stresses in transversal direction are close to the measured ones.

- The predicted longitudinal residual stresses are close to the measured ones for a depth higher than about 20 μm below the surface.
- The thickness of the layer affected by residual stresses due to machining (*Layer_RS*) is very well predicted.

The simulated and measured residual stresses at machined surface (SRS) for all the conditions are shown in Fig. 13. As mentioned above, the difference between simulated and

Fig. 14 Simulated and measured maximum residual stresses below the machined surface maximum (MRS)

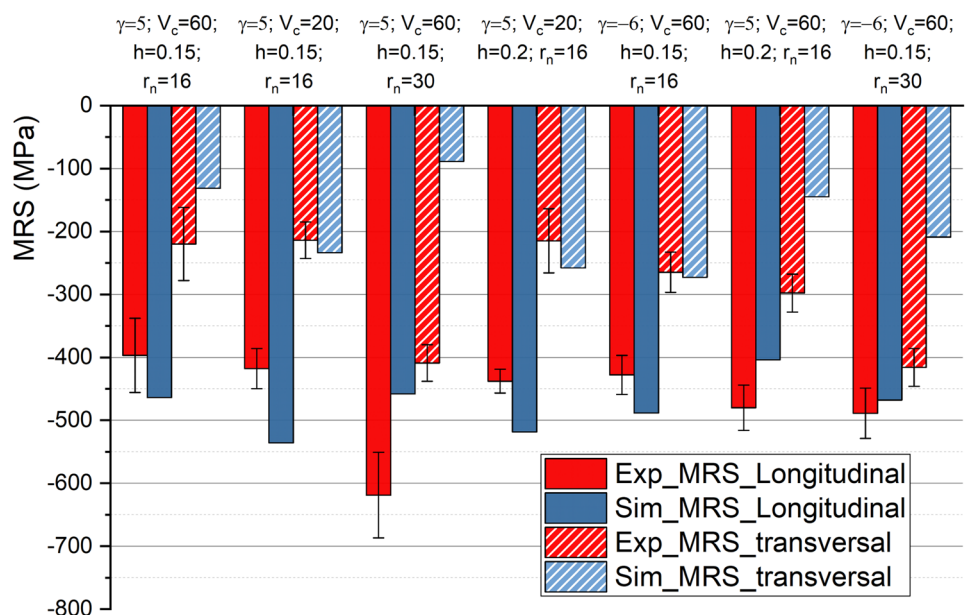
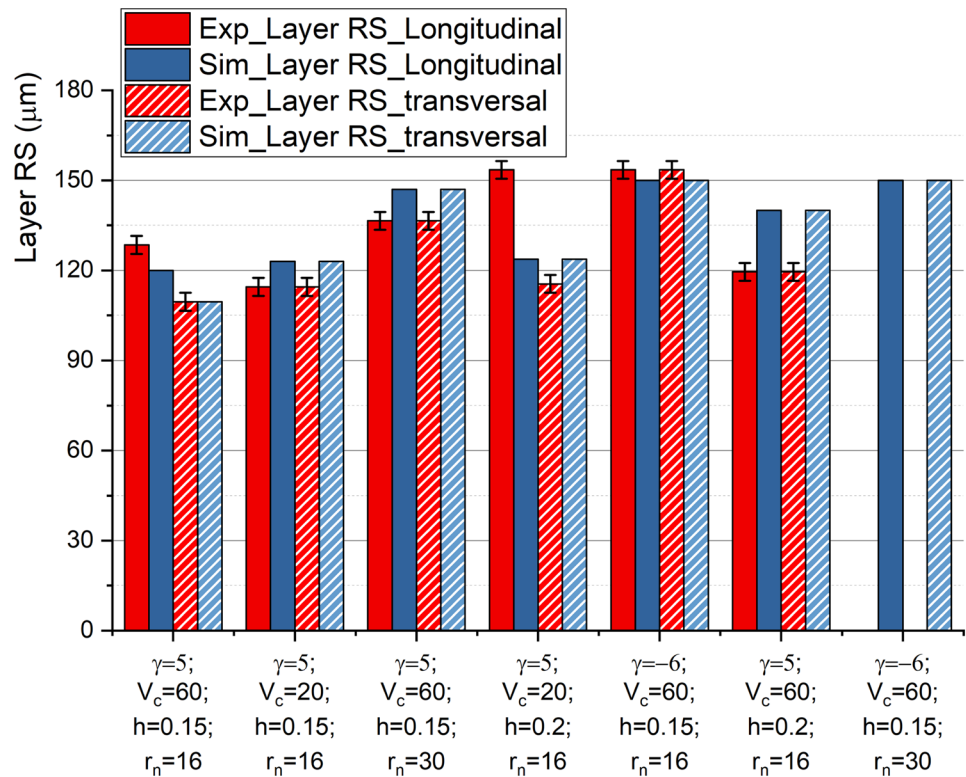


Fig. 15 Simulated and measured thickness of the layer affected by residual stresses induced by orthogonal cutting (*Layer_RS*)



measured *SRS* in longitudinal direction is significant. However, *SRS* in transversal direction is better predicted than that in the longitudinal direction, although the difference between simulated and measured *SRS* in transversal direction is high for half of the investigated cutting conditions.

Figure 14 shows the simulated and measured *MRS* in compression beneath the surface for all the conditions. The difference between simulated and measured *MRS* in transversal direction can reach about 36% in average, while in the longitudinal direction this difference is only about 17% in average. Therefore, the *MRS* is reasonably well predicted by numerical simulation.

Figure 15 presents the simulated and measured thickness of the layer affected by residual stresses induced by orthogonal cutting (*Layer_RS*). In general, this thickness is quite well predicted by the simulation, where the maximum difference between predicted and measured thicknesses is less than 19%. Fig. 15.

The observed differences between the measured and predicted residual stress profiles, in particular near the machined surface, can be attributed to the distortion of the elements near the machined surface during the cutting simulation. These distorted elements affect the values of the residual stresses near the surface in the longitudinal direction. Another reason already mentioned above is the tool-workpiece contact, which is unable to reproduce the exact contact stresses between the tool and the machined surface. Finally, although the temperature in the FDZ is around 220 °C (see Fig. 6d), thus not affecting the

mechanical behaviour of the work material in this region, the temperature in the TDZ can reach 300 °C, according to the simulations (see Fig. 6d). These predicted values of temperature in the TDZ need to be confirmed by accurate temperature measurements, since the excessive distortion of the elements of the machined surface will also affect the temperature prediction in this surface. If these measurements confirm these temperature values, then the temperature effect must also be considered in the constitutive model for better residual stress prediction.

5 Conclusions

2D orthogonal cutting model of Ti-6Al-4 V alloy was developed and simulated using the finite element method and the Lagrangian approach implemented in ABAQUS FEA software. The cutting model included the proposed constitutive model proposed by Cheng et al. [39] considering the SoT. This constitutive model was implemented in ABAQUS FEA software through a VUMAT and UMAT subroutines. The orthogonal cutting model is composed by the tool, workpiece and an intermediate layer where the element deletion technique is applied to simulate the physical separation of the layer being removed (in the form of chips) from the rest of the workpiece. The contact conditions at the tool-chip and the tool-workpiece interfaces were modelled using the Zorev's model and using the friction coefficient in function

of the sliding speed. Coupled thermo-mechanical analysis was performed to predict the cutting and thrust forces, chip geometry, chip compression ratio, temperature distribution in the cutting zone and residual stress distributions in the machined surface and subsurface.

To evaluate the accuracy of the orthogonal cutting model including the proposed constitutive model considering the SoT, the predicted results using this model are compared with those obtained from orthogonal cutting tests (forces, chip geometry and chip compression ratio) and X-ray diffraction analysis (residual stresses at the machined samples) for seven cutting conditions. The cutting force is relatively well predicted for all these cutting conditions, where the difference between the measured and predicted values was less than 14%. However, as it is also been observed in metal cutting simulations [14, 34], the thrust force is underestimated, and the difference between measured and predicted value is about 53%. The parameters of the chip geometry (peak and pitch) are reasonably predicted, except the chip valley that is over estimated (differences between measured and predicted values can reach about 51%). The predicted in-depth residual stress profiles in longitudinal direction are closer to the experimental ones when the depth beneath the surface is greater than 20 μm . However, they are significantly different in the transversal direction for three out of seven cutting conditions. Additionally, the difference between the simulated and measured maximum residual stress in compression beneath the surface in the transversal direction is about 36% in average, while in the longitudinal direction this difference reduces to about 17% in average. Finally, the maximum difference between the predicted and measured thicknesses of the layer affected by the residual stresses due to machining is less than 19%.

The predicted cutting force and chip geometry obtained using the proposed constitutive model considering the SoT are also compared with the cutting force and chip geometry obtained using the proposed constitutive model but without considering the SoT and using the *J-C* one. This comparison shows that the orthogonal cutting model including the proposed constitutive model considering the SoT predicts better the cutting forces and chip geometry than the other cutting models.

The differences between the predicted and measured results can be mainly due to the incorrect description of the tool-workpiece contact and to the significant mesh distortion typical of the Lagrangian approach. Therefore, the contact model should be improved to better represent the tool-workpiece contact. In addition, although the temperature does not affect the mechanical behaviour of the work material in the FDZ, it may affect the mechanical behaviour in the TDZ, and, consequently, the residual stress prediction. Therefore, thermal effect should be added to the constitutive model considering the SoT for

an accurate prediction of the residual stresses near the surface. Finally, another numerical approach should be used to simulate the chip formation in the metal cutting, which should minimize mesh distortion and better simulate the tool-workpiece contact.

Acknowledgements The authors would like to thank Dr. Bertrand Marcon from Arts & Metiers Institute of Technology for his help in the digital image correlation system.

Funding The research work presented in the article was financially supported by Seco Tools and Safran companies and China Scholarships Council program (No. 201606320213).

Declarations

Ethics approval Not applicable.

Consent to participate Not applicable.

Consent for publication We authorize the publication of this research work.

Conflict of interest The authors declare no competing interests.

References

- Leyens C, Peters M (2005) Titanium and titanium alloys: fundamentals and applications. Wiley-VCH Verlag
- Arrazola P-J, Garay A, Iriarte L-M et al (2009) Machinability of titanium alloys (Ti6Al4V and Ti555.3). *J Mater Process Technol* 209:2223–2230. <https://doi.org/10.1016/j.jmatprotec.2008.06.020>
- Liang X, Liu Z, Wang B (2019) State-of-the-art of surface integrity induced by tool wear effects in machining process of titanium and nickel alloys: a review. *Measurement* 132:150–181. <https://doi.org/10.1016/j.measurement.2018.09.045>
- M'Saoubi R, Outeiro JC, Chandrasekaran H et al (2008) A review of surface integrity in machining and its impact on functional performance and life of machined products. *Int J Sustain Manuf* 1:203. <https://doi.org/10.1504/IJSM.2008.019234>
- Niknam SA, Khettabi R, Songmene V (2014) Machinability and machining of titanium alloys: a review. In: Davim JP (ed) *Machining of titanium alloys*. Springer, Berlin, Heidelberg, pp 1–30
- Ulutan D, Ozel T (2011) Machining induced surface integrity in titanium and nickel alloys: a review. *Int J Mach Tools Manuf* 51:250–280. <https://doi.org/10.1016/j.ijmactools.2010.11.003>
- Ezugwu EO, Wang ZM (1997) Titanium alloys and their machinability—a review. *J Mater Process Technol* 68:262–274. [https://doi.org/10.1016/S0924-0136\(96\)00030-1](https://doi.org/10.1016/S0924-0136(96)00030-1)
- Jawahir IS, Brinksmeier E, M'Saoubi R et al (2011) Surface integrity in material removal processes: recent advances. *CIRP Ann - Manuf Technol* 60:603–626. <https://doi.org/10.1016/j.cirp.2011.05.003>
- Denguir LA, Outeiro JC, Fromentin G (2020) Multi-physical analysis of the electrochemical behaviour of OFHC copper surfaces obtained by orthogonal cutting. *Corros Eng Sci Technol* 1–10. <https://doi.org/10.1080/1478422X.2020.1836879>
- Wang Q, Liu Z, Wang B et al (2016) Evolutions of grain size and micro-hardness during chip formation and machined surface generation for Ti-6Al-4V in high-speed machining. *Int J Adv Manuf Technol* 82:1725–1736. <https://doi.org/10.1007/s00170-015-7508-1>

11. Sun J, Guo YB (2009) A comprehensive experimental study on surface integrity by end milling Ti–6Al–4V. *J Mater Process Technol* 209:4036–4042. <https://doi.org/10.1016/j.jmatprotec.2008.09.022>
12. Holmberg J, Rodríguez Prieto JM, Berglund J et al (2018) Experimental and PFEM-simulations of residual stresses from turning tests of a cylindrical Ti-6Al-4V shaft. *Procedia CIRP* 71:144–149. <https://doi.org/10.1016/j.procir.2018.05.087>
13. Pan Z, Shih DS, Garmestani H, Liang SY (2019) Residual stress prediction for turning of Ti-6Al-4V considering the microstructure evolution. *Proc Inst Mech Eng Part B J Eng Manuf* 233:109–117. <https://doi.org/10.1177/0954405417712551>
14. Rotella G, Umbrello D (2014) Finite element modeling of microstructural changes in dry and cryogenic cutting of Ti6Al4V alloy. *CIRP Ann - Manuf Technol* 63:69–72. <https://doi.org/10.1016/j.cirp.2014.03.074>
15. Hong SY, Markus I, Jeong W (2001) New cooling approach and tool life improvement in cryogenic machining of titanium alloy Ti-6Al-4V. *Int J Mach Tools Manuf* 41:2245–2260
16. Hong SY, Ding Y (2001) Cooling approaches and cutting temperatures in cryogenic machining of Ti-6Al-4V. *Int J Mach Tools Manuf* 41:1417–1437
17. Ayed Y, Germain G, Melsio AP et al (2017) Impact of supply conditions of liquid nitrogen on tool wear and surface integrity when machining the Ti-6Al-4V titanium alloy. *Int J Adv Manuf Technol* 93:1199–1206. <https://doi.org/10.1007/s00170-017-0604-7>
18. Jamil M, Khan AM, Gupta MK et al (2020) Influence of CO₂-snow and subzero MQL on thermal aspects in the machining of Ti-6Al-4V. *Appl Therm Eng* 177:115480. <https://doi.org/10.1016/j.applthermaleng.2020.115480>
19. Kara F, Aslantaş K, Çiçek A (2016) Prediction of cutting temperature in orthogonal machining of AISI 316L using artificial neural network. *Appl Soft Comput* 38:64–74
20. Kara F, Aslantaş K, Çiçek A (2015) ANN and multiple regression method-based modelling of cutting forces in orthogonal machining of AISI 316L stainless steel. *Neural Comput Appl* 26:237–250. <https://doi.org/10/f6vj7>
21. Outeiro JC, Umbrello D, M'Saoubi R, Jawahir IS (2015) Evaluation of present numerical models for predicting metal cutting performance and residual stresses. *Mach Sci Technol* 19:183–216. <https://doi.org/10.1080/10910344.2015.1018537>
22. Zorev NN (1966) *Metal cutting mechanics*. Pergamon Press, Oxford, p 1966
23. Dirikolu MH, Childs THC, Maekawa K (2001) Finite element simulation of chip ow in metal machining. *Int J Mech Sci* 15. <https://doi.org/10/dd3xcv>
24. Courbon C, Pusavec F, Dumont F et al (2013) Tribological behaviour of Ti6Al4V and Inconel718 under dry and cryogenic conditions—application to the context of machining with carbide tools. *Tribol Int* 66:72–82. <https://doi.org/10.1016/j.triboint.2013.04.010>
25. Melkote SN, Grzesik W, Outeiro J et al (2017) Advances in material and friction data for modelling of metal machining. *CIRP Ann* 66:731–754. <https://doi.org/10.1016/j.cirp.2017.05.002>
26. Chen L, El-Wardany TI, Harris WC (2004) Modelling the Effects of flank wear land and chip formation on residual stresses. *CIRP Ann - Manuf Technol* 53:95–98. [https://doi.org/10.1016/S0007-8506\(07\)60653-2](https://doi.org/10.1016/S0007-8506(07)60653-2)
27. Zang J, Zhao J, Li A, Pang J (2018) Serrated chip formation mechanism analysis for machining of titanium alloy Ti-6Al-4V based on thermal property. *Int J Adv Manuf Technol* 98:119–127. <https://doi.org/10.1007/s00170-017-0451-6>
28. Huang Y, Ji J, Lee K-M (2018) An improved material constitutive model considering temperature-dependent dynamic recrystallization for numerical analysis of Ti-6Al-4V alloy machining. *Int J Adv Manuf Technol* 97:3655–3670. <https://doi.org/10.1007/s00170-018-2210-8>
29. Calamaz M, Coupard D, Girof F (2008) A new material model for 2D numerical simulation of serrated chip formation when machining titanium alloy Ti–6Al–4V. *Int J Mach Tools Manuf* 48:275–288. <https://doi.org/10.1016/j.ijmactools.2007.10.014>
30. Karpat Y (2011) Temperature dependent flow softening of titanium alloy Ti6Al4V: an investigation using finite element simulation of machining. *J Mater Process Technol* 211:737–749. <https://doi.org/10.1016/j.jmatprotec.2010.12.008>
31. Sima M, Özel T (2010) Modified material constitutive models for serrated chip formation simulations and experimental validation in machining of titanium alloy Ti–6Al–4V. *Int J Mech Sci* 50:943–960. <https://doi.org/10.1016/j.ijmactools.2010.08.004>
32. Ducobu F, Rivière-Lorphèvre E, Filippi E (2016) Material constitutive model and chip separation criterion influence on the modeling of Ti6Al4V machining with experimental validation in strictly orthogonal cutting condition. *Int J Mech Sci* 107:136–149. <https://doi.org/10.1016/j.ijmecsci.2016.01.008>
33. Röhlin M, Klippel H, Afrasiabi M, Wegener K (2019) Metal cutting simulations using smoothed particle hydrodynamics on the GPU. *Int J Adv Manuf Technol*. <https://doi.org/10.1007/s00170-019-03410-0>
34. Vijay Sekar KS, Pradeep Kumar M (2011) Finite element simulations of Ti6Al4V titanium alloy machining to assess material model parameters of the Johnson-Cook constitutive equation. *J Braz Soc Mech Sci Eng* 33:203–211. <https://doi.org/10.1590/S1678-58782011000200012>
35. Fernandez-Zelaia P, Melkote S, Marusich T, Usui S (2017) A microstructure sensitive grain boundary sliding and slip based constitutive model for machining of Ti-6Al-4V. *Mech Mater* 109:67–81. <https://doi.org/10.1016/j.mechmat.2017.03.018>
36. Yameogo D, Haddag B, Makich H, Nouari M (2019) A physical behavior model including dynamic recrystallization and damage mechanisms for cutting process simulation of the titanium alloy Ti-6Al-4V. *Int J Adv Manuf Technol* 100:333–347. <https://doi.org/10.1007/s00170-018-2663-9>
37. Xu X, Zhang J, Outeiro J et al (2020) Multiscale simulation of grain refinement induced by dynamic recrystallization of Ti6Al4V alloy during high speed machining. *J Mater Process Technol* 286:116834. <https://doi.org/10.1016/j.jmatprotec.2020.116834>
38. Wang B, Liu Z (2016) Evaluation on fracture locus of serrated chip generation with stress triaxiality in high speed machining of Ti6Al4V. *Mater Des* 98:68–78. <https://doi.org/10.1016/j.matdes.2016.03.012>
39. Cheng W, Outeiro J, Costes J-P et al (2019) A constitutive model for Ti6Al4V considering the state of stress and strain rate effects. *Mech Mater* 137:103103. <https://doi.org/10.1016/j.mechmat.2019.103103>
40. Xu X, Outeiro J, Zhang J et al (2021) Machining simulation of Ti6Al4V using coupled Eulerian-Lagrangian approach and a constitutive model considering the state of stress. *Simul Model Pract Theory* 110:102312. <https://doi.org/10.1016/j.simpat.2021.102312>
41. ASTM E3 - 11 (2017) Standard guide for preparation of metallographic specimens. ASM International
42. Astakhov VP, Shvets S (2004) The assessment of plastic deformation in metal cutting. *J Mater Process Technol* 146:193–202. <https://doi.org/10.1016/j.jmatprotec.2003.10.015>
43. Noyan IC, Cohen JB (1987) *Residual stress - measurement by diffraction and interpretation*. Society for Experimental Mechanics, Springer-Verlag, New York
44. Kops L, Arenson M (1999) Determination of convective cooling conditions in turning. *CIRP Ann* 48:47–52. [https://doi.org/10.1016/S0007-8506\(07\)63129-1](https://doi.org/10.1016/S0007-8506(07)63129-1)
45. Cheng W, Outeiro J, Costes J-P et al (2019) Optimization-based procedure for the determination of the constitutive model coefficients used in machining simulations. *Procedia CIRP* 82:374–378. <https://doi.org/10.1016/j.procir.2019.04.057>

46. Zorev NN (1966) Metal cutting mechanics. Pergamon Press, Oxford
47. Astakhov VP, Outeiro JC (2008) Metal cutting mechanics, finite element modelling. In: Davim JP (ed) Machining: fundamentals and recent advances. Springer
48. Outeiro JC (2020) Residual stresses in machining. In: Mechanics of materials in modern manufacturing methods and processing technique, V. Silberschmidt. Elsevier
49. Astakhov VP (2006) Tribology of Metal Cutting. Elsevier
50. Chen G, Ren C, Yang X et al (2011) Finite element simulation of high-speed machining of titanium alloy (Ti–6Al–4V) based on ductile failure model. *Int J Adv Manuf Technol* 56:1027–1038. <https://doi.org/10.1007/s00170-011-3233-6>
51. Zhang YC, Mabrouki T, Nelias D, Gong YD (2011) Chip formation in orthogonal cutting considering interface limiting shear stress and damage evolution based on fracture energy approach. *Finite Elem Anal Des* 47:850–863
52. Li A, Pang J, Zhao J et al (2017) FEM-simulation of machining induced surface plastic deformation and microstructural texture evolution of Ti-6Al-4V alloy. *Int J Mech Sci* 123:214–223. <https://doi.org/10.1016/j.ijmecsci.2017.02.014>
53. Abushawashi Y, Xiao X, Astakhov V (2017) Practical applications of the “energy–triaxiality” state relationship in metal cutting. *Mach Sci Technol* 21:1–18. <https://doi.org/10.1080/10910344.2015.1133913>

Publisher's Note Springer Nature remains neutral with regard to jurisdictional claims in published maps and institutional affiliations.